

# Framework for shape analysis of white matter fiber bundles

Tanya Glozman<sup>a,\*</sup>, Lisa Bruckert<sup>b</sup>, Franco Pestilli<sup>c</sup>, Derek W. Yecies<sup>d</sup>, Leonidas J. Guibas<sup>e,1</sup>, Kristen W. Yeom<sup>f,1</sup>

<sup>a</sup> Electrical Engineering, Stanford University, Stanford, CA, USA

<sup>b</sup> Pediatrics, Stanford University, Stanford, CA, USA

<sup>c</sup> Psychological and Brain Sciences, Indiana University, Bloomington, IN, USA

<sup>d</sup> Pediatric Neurosurgery, Stanford University, Stanford, CA, USA

<sup>e</sup> Computer Science, Stanford University, Stanford, CA, USA

<sup>f</sup> Department of Radiology, Lucile Packard Children's Hospital, Stanford University, Stanford, CA, USA

## ARTICLE INFO

### Keywords:

White matter  
Shape analysis  
Development

## ABSTRACT

Diffusion imaging coupled with tractography algorithms allows researchers to image human white matter fiber bundles in-vivo. These bundles are three-dimensional structures with shapes that change over time during the course of development as well as in pathologic states. While most studies on white matter variability focus on analysis of tissue properties estimated from the diffusion data, e.g. fractional anisotropy, the *shape* variability of white matter fiber bundle is much less explored. In this paper, we present a set of tools for shape analysis of white matter fiber bundles, namely: (1) a concise geometric model of bundle shapes; (2) a method for bundle registration between subjects; (3) a method for deformation estimation. Our framework is useful for analysis of shape variability in white matter fiber bundles. We demonstrate our framework by applying our methods on two datasets: one consisting of data for 6 normal adults and another consisting of data for 38 normal children of age 11 days to 8.5 years. We suggest a robust and reproducible method to measure changes in the shape of white matter fiber bundles. We demonstrate how this method can be used to create a model to assess age-dependent changes in the shape of specific fiber bundles. We derive such models for an ensemble of white matter fiber bundles on our pediatric dataset and show that our results agree with normative human head and brain growth data. Creating these models for a large pediatric longitudinal dataset may improve understanding of both normal development and pathologic states and propose novel parameters for the examination of the pediatric brain.

## Introduction

Advances in diffusion magnetic resonance imaging (dMRI) and tractography methods now allow in-vivo high resolution imaging of human white matter (WM) and extraction of the brain connectome - a large collection of WM fibers. As increasing numbers of dMRI datasets become publicly available, much of the recent work in the neuroscientific community revolves around analysis of specific WM bundles - subsets of fibers - with regards to population comparison, lateralization and neurological disorders. Most studies of WM variability focus on analysis of tissue properties estimated by different values extracted from the diffusion data, such as Fractional Anisotropy. The shape variability of white matter, however, is much less studied. The paucity of investigation into white matter shape is due to several factors. It is in part due to the

fact that the shape of fiber bundles is irregular and complex, and in part because there are still ongoing debates in the community regarding the ambiguous nature of tractography methods used to extract these structures. WM fiber bundles are essentially three-dimensional geometric structures with origination and termination regions, anatomically constrained by adjacent brain structures. Their geometric shape has been confirmed by postmortem brain anatomy studies, e.g. [Mori et al., 2017](#), and atlases have been constructed that determine both the common shape and the common location of different fiber bundles, [Wakana et al., 2004](#). At present, shape morphology of WM fiber bundles over the course of normal development and pathologic states represents an unexplored area of investigation that may yield new insights into normal and pathologic brain development. Specifically, the lack of normative data in the pediatric population has constrained efforts to create normal atlases of

\* Corresponding author.

E-mail address: [tanyagl@stanford.edu](mailto:tanyagl@stanford.edu) (T. Glozman).

<sup>1</sup> L. Guibas and K. Yeom are Co-Principal Investigators in this work. LG oversaw the method development and KY oversaw the imaging data collection.

pediatric brain development using any imaging modality, including WM imaging. This paper aims to address this gap and presents a framework of computational geometry tools focused on analyzing the shape variability of WM fiber bundles. We present: (1) a concise and novel geometric model for fiber bundle shapes, (2) spatial correspondence mapping between regions of interest on homologous fiber bundles, (3) registration of fiber bundles across subjects in bundle space, and (4) bundle deformation estimation. To demonstrate the abilities of our framework, we apply our methods to a unique cross-sectional dataset of 38 healthy children aged 0–8 years and show how it can be used to model the shape change of WM fiber bundles among subjects of different age. Applying the proposed methods to a large longitudinal pediatric dataset, may provide a novel set of parameters for monitoring pediatric brain development.

## Background

### Geometric model of WM fiber bundles

As imaging resolution advances and the extracted connectomes become more and more dense, a need for concise representation of these fiber sets is pressing. In recent years, there have been several efforts to address this need. A method using hierarchical clustering to compress fiber sets by combining analysis in the image space with analysis in fiber space was presented by Guevara et al. (2011). Garyfallidis et al., 2012, presented QuickBundles - a method that reduces fiber clusters to a single centroid streamline. Colby et al., 2012, presented a centralized streamline model for a fiber bundle by assuming that they are tube-like structures with cross-sectional uniformity. Corouge et al., 2004, proposed a clustering scheme that uses the similarity of adjacent curves to group sets of curves to bundles. In this representation, fiber bundles are modeled by a shape prototype swept along a space trajectory. Gori et al., 2016, proposed a weighted prototype scheme for fiber bundles in which several 'prototype' fibers are chosen among the streamlines to represent groups of similar streamlines. Alexandroni et al., 2016, compared hierarchical clustering methods with different distance metrics to the Coresets approach (Agarwal et al., 2005), and showed the superiority of the latter in fiber set reduction. The underlying goal of all these methods is data compression - they aim to eliminate redundancies and find the set of representative fibers of a bundle. This reduction is lossy - in the sense that the fine-detailed geometric shape information is lost in the final representation. In contrast to those methods, Durrleman et al., 2011, proposed using the framework of currents as a metric for analysis of white matter fiber bundles. In this representation, a fiber is represented as a path integral over a vector field which keeps the geometric information of the bundle. The compression ratio that this representation achieves varies with the parameters chosen which control the approximation error. They measure the compression ratio by the number of 'momenta' - 3D vectors (represented by 6 floating point numbers - three for location and three for direction) and report 85% compression ratio on average. This is not a fixed-length representation as the number of momenta varies with the size of the dataset and the complexity of the geometry of the fiber bundle. Their work achieves impressive results for registration and variability analysis. Some efforts are also aimed at characterizing the shape of fiber bundles: Batchelor et al., 2006, used fundamental geometric invariants such as curvature and torsion to estimate an 'average' shape for several human fiber bundles. Similarly to Durrleman et al., 2011, our geometric model achieves data compression without compromising the completeness of geometry information. It creates a concise representation of the shape of the fiber bundles, allowing shape analysis at a fine scale as well as bundle registration and deformation estimation. Furthermore, our model achieves fixed-length representation, regardless of the number of subjects in the dataset, or the number of fibers in the analyzed bundles. Our geometric model for a fiber bundle consists of a fixed number,  $X$ , of 3D Seed Points (three floating point numbers per Seed Point), where  $X$  is determined by the user according to how fine the analysis should be. Since the length and complexity of WM fiber bundles varies greatly within subjects as well as across populations, the ability to adjust the

scope of the analysis is essential and useful for different investigations. In the experiments we show in this paper, we chose  $X = 340$ . The number of nodes in fiber bundles varies, but is usually in the several thousands - thus our representation constitutes a compression ratio of well over 90% on average. The fact that our representation is of fixed length renders it useful for many different types of group analyses and algorithms.

### Registration

Most available methods for group analysis of white matter still rely on whole-brain image-based registration, such as Smith et al., 2006, and Ashburner and Friston, 2000. These methods find the optimal diffeomorphic registration by minimizing cost-functions defined on voxels. In dMRI processing, scalar diffusivity measures, such as Fractional Anisotropy (FA) values serve as the basis for registration, e.g. in Groeschel et al. (2014). The whole-brain registration approach, however, has several challenges when the data analyzed is of brains with 'non-typical' gray-level appearance, such as a presence of a mass lesion in the form of a tumor, vascular malformation, abscess, hemorrhage, or brain deformation that might be associated with hydrocephalus. In these cases, since this form of registration relies on the full brain volume for alignment, the abnormal area may cause the registration to fail. Low intensity or poor contrast may also lead to poor results. Additionally, these methods rely on the assumption that the shape variability of white matter fiber bundles is reflected in the variability of diffusivity measures. Most diffusivity measures, however, rely on the diffusion tensor model, which possesses a single major orientation. As a result, this model cannot adequately describe white matter regions that contain two or more differently oriented fiber bundles within the same voxel (crossing, diverging, or kissing fibers) leading to incorrect estimations of diffusion measures and fiber directions Pierpaoli et al., 2001, Alexander et al., 2002, Descoteaux et al., 2009. Thus image-based registration doesn't necessarily correctly align the neural pathways. Sotiras et al., 2013, provides an excellent review of methods used for registration in the medical imaging domain. In this work the authors conclude that registration becomes more robust even under the existence of large deformations once *landmarks* are established. In dMRI imaging such landmarks are the white matter fiber bundles. Indeed, recently there have been much research in this direction - registration in the space of bundles (the anatomical landmarks), rather than in image space. In these methods, the fiber bundles extracted from the dMRI data are treated as stand-alone shapes, and the goal for the registration is to align these shapes across subjects, independently of the tractography algorithms used for their estimation. In Garyfallidis et al. (2015), the authors presented the Streamline-based Linear Registration framework that registers homologous bundles by minimizing a cost function based on local and global geometric properties of the bundles, without using any geometric model for the bundles themselves. They define a distance metric between two bundles that accounts for all the points on the fibers (streamlines) to drive the registration. O'Donnell et al., 2012, proposed to directly register whole tractograms without the indirect step of whole-volume image registration by minimizing a loss function computed only from a random subset of streamline coordinates. Olivetti et al., 2016, find an optimal correspondence between streamlines of one tractogram to streamlines in another in a similar manner to the graph matching problem. Siless et al., 2017, proposed a way to cluster tractography streamlines based on their neighboring anatomical structures, rather than their coordinates, achieving a registration free analysis method across subjects. Zvitia et al., 2010, use Gaussian Mixture Models to represent fiber sets, which are registered by maximizing their correlation ratio. Fishbaugh et al., 2014, proposed a framework based on currents to model and register fiber bundles. The work presented in this paper falls within this category of bundle-space registration.

### Methods

Diffusion MRI allows imaging the neuroanatomy of white matter structures in-vivo. When comparing the anatomy and function of these

structures across populations, it is important to establish spatial correspondence between different sets of tractography data. Such correspondence maps drive the registration (i.e. non-rigid spatial alignment) between the different fiber bundles, from which the shape deformation can be estimated. In this section, we present the full framework for shape analysis of white matter bundles. This framework consists of methods for: (a) creating a geometric model of a WM fiber bundle (section [Geometric model of a fiber bundle](#)); (b) fine-scale correspondence mapping between bundles of different subjects (section [Fine-scale correspondence mapping between fiber bundles of different subjects](#)); (c) free-form registration for bundle alignment (section [Fiber bundle registration](#)); and (d) shape deformation estimation (section [Shape deformation estimation](#)). Each step is built upon the previous steps.

#### Fiber bundle representation and pre-processing

Following tractography processing as elaborated in section [Data for experiments](#), the data for each bundle is represented as a fiber bundle - a set of  $N$  fibers  $\{f_i\}_{i=1}^N$ , each fiber consisting of  $M_i$  points in  $\mathbb{R}^3$   $[x_j, y_j, z_j]_{j=1}^{M_i}$ . Each fiber is then resampled to  $L$  points, where  $L$  is chosen by the user. For longer fiber bundles with elaborate geometry a higher  $L$  should be chosen (e.g.  $L = 100$ ), while for shorter bundles a smaller  $L$  suffices. In this work we chose  $L = 60$ . Following the resampling, fibers are flipped such that all  $[x_1, y_1, z_1]$  points are on one end of the bundle and all  $[x_L, y_L, z_L]$  points are at another end of the bundle. Following the resampling, we calculate the Centerline - an 'average' fiber that follows the curvature of the bundle. The Centerline is a curve consisting of  $L$  points  $[C_{x_j}, C_{y_j}, C_{z_j}]_{j=1}^L$  where each point is an average of all the points with the same index on all the fibers, calculated as follows:  $[C_{x_j}, C_{y_j}, C_{z_j}] = \frac{1}{N} \sum_{i=1}^N [x_j, y_j, z_j]$ .

#### Geometric model of a fiber bundle

Homologous fiber bundles of different subjects may have different shape both in the macro-level and in fine-level details: they may differ in the number of fibers, average length of the fibers, cross-sectional areas along the bundle, the distribution of the fibers within a cross-section etc. We suggest a model that represents the variable geometry of such bundles in a way that is both concise and allows for correspondence mapping between regions of interest on bundles from different subjects. The fundamental observation that guides our model is that the geometry of a bundle has two components - along the fibers and across the fibers. Along the fibers length, the bundle has many fibers aligned in roughly the same direction. At every point along this main direction, a cross-section contains nodes of all the fibers at that point. Our framework models these two components. Our representation for a fiber bundle is a set of *Seed Points*  $\{c_i\}_{i=1}^C$ . This is a fixed-length representation, since all bundles are represented using the same number of Seed Points. Moreover, the representation is consistent, such that Seed Point  $c_i^A$  of bundle A and Seed Point  $c_i^B$  on bundle B are located in corresponding regions on their respective bundles. [Alg. 1](#) outlines the process for calculating the representation. As the model essentially creates a division of a bundle into regions, we refer to this process as *fiber bundle parcellation*. The input to the parcellation algorithm is the fiber bundle, with its fibers resampled and flipped as previously explained. The output is a set of  $C$  *Seed Points* that capture the geometry of the fiber bundle. This is achieved by the following steps:

1. The Centerline that follows the mean curvature of the fiber bundle is calculated (as explained in section [Fiber bundle representation and pre-processing](#)).
2.  $K$  uniformly spaced (according to geodesic distance) locations along the Centerline are chosen  $\{c_i\}_{i=1}^K$  ( $K$  is a user-chosen parameter according to the desired parcellation resolution).

3. The local Centerline direction  $\vec{c}_i$  is calculated at each location.
4. Two points above and below  $c_i$  along  $\vec{c}_i$ , namely  $c_i^+$  and  $c_i^-$  are found. These points are chosen such that  $c_i^+ < c_{i+1}^-$  and  $c_i^- > c_{i-1}^+$ , effectively creating non-overlapping ranges along the centerline.
5. Two planes perpendicular to the Centerline direction are defined using the local centerline direction  $\vec{c}_i$  as normal and the points  $c_i^+$  and  $c_i^-$  respectively.
6. The area between these two planes defines a 'slab'. An example of a 'slab' can be seen in [Fig. 2](#) (b). All the nodes on the fibers that are contained within such 'slab' create a point-cloud shaped roughly as a short cylinder with an elliptical cross-section.
7. All nodes in the slab are projected to a cross-sectional plane in the middle of the cylinder to get a 2D ellipsoid. The axes of this ellipsoid are calculated.
8. The elliptical slab is then partitioned into  $S$  equal-angle slices.
9. The radius of each slice is determined by the node farthest from the corresponding centerline point for that slice.
10.  $P$  Seed Points are placed on each slice, equally spaced, along a radial line passing in the middle of the slice. This creates a total of  $S \times P$  Seed Points per cross-section.

The model is controlled by four parameters:  $L$  - the number of nodes per fiber (defining the distance between nodes on the fiber),  $K$  - number of cross-sections per bundle (defining the number of 'slabs' per fiber bundle,  $K < L$ ),  $S$  - number of slices per cross-section (defining the number of angular slices each 'slab' is cut into) and  $P$  - number of Seed Points per slice (defining the number of clusters in each slice). These can be set by the user based on the required correspondence mapping accuracy. A different set of parameters results in a different parcellation scheme, with the resulting cluster locations visually consistent across subjects. Thus for datasets produced by higher resolution white matter imaging methods, or when finer detailed correspondence mapping is required the user may choose to use finer resolution for the shape analysis - requiring more Seed Points. When a coarser analysis is sufficient the user may choose parameters that yield less Seed Points in the model. In this experiment we chose the following parameters:  $K = 20$  (number of cross-sections),  $S = 8$  (number of slices per cross-section) and  $P = 2$  (number of Seed Points per slice). This choice of parameters yields  $8 \times 2 = 16$  Seed Points per cross-section, resulting in a total  $(20 \times 16) + 20 = 340$  Seed Points, thus 340 clusters. For a finer or coarser analysis this number can be set by the user. An overview of the parcellation process for the left thalamic radiation (LTR) fiber bundle is shown in [Fig. 1](#). The bundle itself is shown on the left. The middle figure shows the locations of the Seed Points, each Seed Point is a centroid of a corresponding cluster. Note that the Seed Points capture the spatial 'spread' of the bundle at each location along the Centerline. The figure on the right shows the result of the parcellation. Points on the fibers are grouped together in clusters based on their spatial location and local geometry using  $K$ -nearest-neighbors algorithm. Each cluster is shown in a different color.

In the illustration in [Fig. 2a](#) we show the fibers (in light gray) with three cross-sectional 'slabs', each with  $s = 8$  slices and  $P = 2$  Seed Points. [Fig. 2b](#) shows an example of one such 'slab' (viewed from above), the nodes belonging to the slab and the assigned Seed Points. This slab was partitioned to  $S = 8$  slices of angle  $45^\circ$  each. This partitioning was chosen empirically as an optimal partitioning to capture the fine geometry variations in the dataset while keeping the number of slices as small as possible. The nodes (points on the fibers) belonging to each slice are shown in different color. The radial extent of each slice determines the placement of Seed Points (black squares on the figure) in that slice. The central Seed Point is placed at the centroid of all the nodes belonging to the slab.

**Algorithm 1.** Fiber Bundle Parcellation.



**Fig. 1. Parcellation overview.** (left) Left Thalamic Radiation (LTR) fiber bundle; (middle) Seed Points representation models the geometry of the bundle. Each node on the bundle is assigned to one of the SeedPoints using a nearest-neighbor approach; (right) parcellated LTR bundle - each color represents a different cluster. Cluster location is visually consistent across subjects in a given dataset.

```

1:  $fibers \leftarrow \text{ResampleAndFlipFibers}(fibers)$ 
2:  $Centerline \leftarrow \text{ExtractCenterline}(fibers)$ 
3: for  $node$  in  $[0, 1, \dots, K]$  on  $Centerline$  do
4:    $NodeDir \leftarrow \text{CalculateDirection}(node, Centerline)$ 
5:   if  $reference$  then
6:      $NodeDirRef \leftarrow NodeDir$ 
7:      $p \leftarrow \text{GetPointsAround}(node)$ 
8:      $V \leftarrow \text{EigenVectors}(p)$ 
9:      $V \leftarrow \text{Normalize}(V)$ 
10:  else
11:     $RotMat \leftarrow \text{CalcRotationMatrix}(NodeDir, NodeDirRef)$ 
12:     $V \leftarrow \text{RotateVectors}(V, RotMat)$ 
13:  end if
14:   $SeedPoints \leftarrow \text{FindSeeds}(V)$ 
15: end for

```

#### Fine-scale correspondence mapping between fiber bundles of different subjects

Given a group of fiber bundles from a dataset of subjects, we are interested in finding the spatial correspondence map between these bundles, i.e. a mapping function that indicates the location of a chosen region of interest (ROI) on bundles from different subjects. Such correspondence map can be used for registration and shape deformation

estimation (as we do in the rest of this paper). It can also be used for shape analysis or fine-grained tissue properties analysis (similar to the profile analysis in Yeatman et al., 2012, only in a much more fine-grained manner, as the correspondences established relate much smaller regions of interest, rather than cross-sections of the bundle). To create the correspondence map for a group of given fiber bundles, we first need to define a reference bundle. A reference can either be a bundle generated by an atlas, or one of the bundles within a given dataset. In this work we arbitrarily chose a fiber bundle of one subject within each dataset as a *reference*. The parcellation of the *reference* bundle informs the parcellation of other bundles in the set, such that the ROIs on all fiber bundles will spatially map to the location of the ROIs on the *reference*. A synthetic reference can also be generated. It is important to note, however, that since the reference bundle serves as a template to which the rest of the bundles are registered, this bundle must have 'sufficient' structure to generate non-null Seed Points model. In this context 'sufficient' means that each cross-section should have at least  $S \times P$  number of points. Within this minor constraint, the choice of the reference does not influence the results. Furthermore, this constraint is rarely not satisfied since the number of fibers generated by tractography algorithms is on the order of several hundreds to a few thousands. For the adult dataset, we randomly chose one of the subjects to serve as reference. For the pediatric dataset, since we were interested in the shape change of fiber bundles among the subjects of different ages, we chose the youngest subject (11 days old) to serve as a reference. The mapping process between a reference bundle

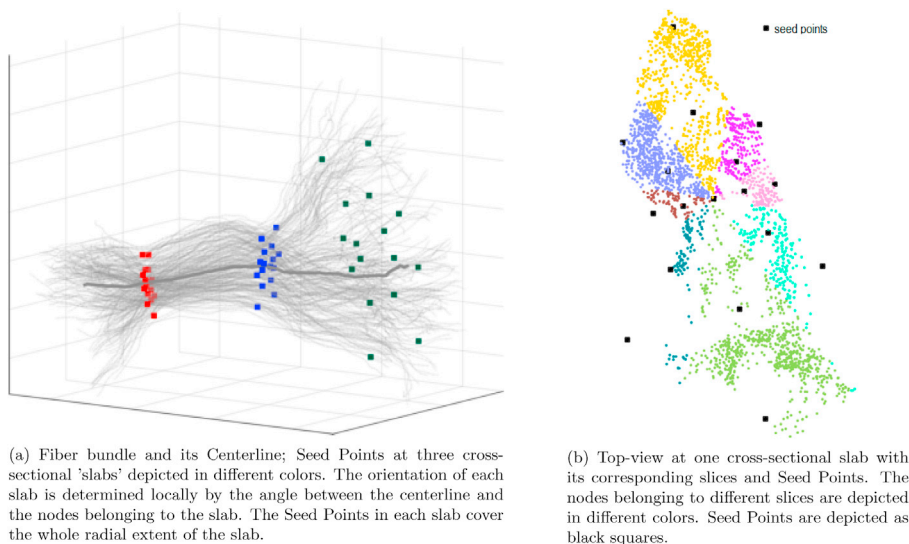


**Fig. 2. Seed Points placement procedure.** The calculated model captures the nature of the fiber bundle shape along the fibers and across the fibers. Left - fiber bundle (thin gray curves) with centerline (thick gray curve) and Seed Points at three cross-sections. Right - top-view on one cross-sectional 'slab'.



and a target bundle is explained in Alg. 1, executing the 'else' statements in lines 11–12. The difference between the reference parcellation and the parcellation of the rest of the bundles in a dataset is in the processing of the cross-sectional 'slabs': the axes of the ellipse model for the slab (the ellipse axes that were calculated on the reference bundle) are multiplied by a rotation matrix (*RotMat*, line 11) formed between the local centerline direction on the moving bundle and the corresponding local centerline direction on the reference bundle. This matrix is calculated by finding a rotation needed to align the two vectors. This operation essentially aligns the axes of the cross sectional ellipse on the moving bundle to its corresponding ellipse on the reference bundle. Following this alignment the algorithm proceeds as before, generating Seed Points. Since all fiber bundles are parcellated similarly, mapping between ROIs is a simple index query operation - given an ROI with index  $j$  on the reference bundle, its corresponding ROI on other bundles in the dataset has the same index  $j$ .

### Fiber bundle registration

One of the major contributions of this work is a method for registration of fiber bundles from different subjects in bundle space. This is enabled by modeling the shape of a fiber bundle by a set of Seed Points, as explained in section [Geometric model of a fiber bundle](#). The Seed Points calculated during the parcellation process constitute the correspondence mapping between the different bundles, as explained in section [Fine-scale correspondence mapping between fiber bundles of different subjects](#). Once such a correspondence is established, we choose a subset of these points as *Control points* to drive the registration. One of the bundles in the dataset is arbitrarily chosen as reference, as discussed in section [Fine-scale correspondence mapping between fiber bundles of different subjects](#). Reference bundle is considered as *fixed* bundle and all other bundles in the set are considered as *moving* bundles and will be registered to the *fixed* bundle. Considering the geometric structure of a fiber bundle, the most significant deformation sources are elongation/shortening along the fibers length and radial expansion/reduction. To account for both these major deformation sources, we propose a two-step registration process whereby the first step consists of registration along the fibers length and the second step consists of the radial registration. Section [Free-form deformation](#) elaborates on the exact process of free-form deformation. An overview of the registration process is as follows:

1. All bundles are preprocessed by (a) resampling all fibers to have equal length; (b) flipping fibers if necessary so that all fibers have the same origin and the same destination.<sup>2</sup>; (c) all bundles are zero-centered.
2. Following the preprocessing, a Centerline for each bundle is calculated as explained in section [Fiber bundle representation and pre-processing](#).
3. A rigid transformation is calculated between to Centerline of the *moving* bundle and the *fixed* bundle. This step consists of finding a rotation matrix,  $R$ , and translation vector,  $T$ , as explained in [Besl and McKay \(1992\)](#).<sup>3</sup>
4. The rotation and translation found in the previous step are applied to all fibers in the *moving* bundle. This results in a very rough alignment between the *moving* and *fixed* bundles.

5. All bundles are parcellated as described in section [Geometric model of a fiber bundle](#) (for the reference) and [Fine-scale correspondence mapping between fiber bundles of different subjects](#) (for the moving bundles).
6. Coarse registration along the fibers length is applied by choosing Centerline Seed Points as Control Points for the free-form registration.
7. Finer 'wireframe' registration is applied by choosing peripheral Seed Points as Control Points for the free-form registration.
8. Post-processing - all fibers are lightly smoothed using a 3-point moving average approach and resampled to keep a fixed distance between points. This step is necessary to avoid spurious fiber curves after the registration.

**Fig. 3** illustrates the control points for the two-step registration. The gray control points are taken from the centerline of the bundle and black control points are on the outer perimeter of the bundle.

### Free-form deformation

Free-form deformation (FFD) by [Sederberg et al. \(1986\)](#), is a method for deforming the shape of an object by transforming the three-dimensional space in which the object is embedded. In this work, B-spline FFD is considered. A 3D grid of regularly spaced b-spline control points is constructed to encapsulate a moving bundle. A set of corresponding points on the reference bundle and on the moving bundle is chosen from our previously found Seed Points. Using quasi-newton optimization we find the deformation of the grid that minimizes the euclidean distance between the correspondence points. The 3D grid is refined during this process to allow better accuracy by doubling the number of points in each dimension. The result of this step is a four-dimensional deformation tensor: for each control point, it contains the displacement (scalar value) and the direction of the displacement (3D vector). Subsequently, we calculate the displacement direction and magnitude for each point of the moving bundle fibers by interpolating between the closest control points. This results in a registration of the moving bundle to the reference bundle.

### Registration accuracy quantification

To quantify registration accuracy we use the Intersection over Union (IoU) measure, also known as Jaccard similarity coefficient (or Jaccard index) [Jaccard, 1901](#). IoU is a normalized measure of overlap and is defined as the size of the intersection divided by the size of the union of two sample sets:  $J(A, B) = \frac{|A \cap B|}{|A \cup B|} = \frac{|A \cap B|}{|A| + |B| - |A \cap B|}$ . The index is 1 when there is a perfect overlap and 0 when there is no overlap. We use this index to quantitatively verify registration accuracy and compare our results to whole-brain image-based registration methods - see section [Comparison with nonlinear whole-brain registration \(WBR\)](#). Since our data is three-dimensional,  $|A \cap B|$  is derived by counting the number of jointly occupied voxels in a 3D grid of a bounding box containing both A and B, while  $|A \cup B|$  is derived by counting the number of singly and doubly occupied voxels in that bounding box, that is voxels occupied by nodes from either A or B or both. To calculate IoU between two bundles A and B, we simply divide between the two counts. We use this measure to compare our registration results to nonlinear whole-brain registration transformation applied on specific fiber bundles (see section [Comparison with nonlinear whole-brain registration \(WBR\)](#)).

### Comparison with nonlinear whole-brain registration (WBR)

To validate our novel fiber-bundle model-based registration (we refer to our method as MBR hereafter), we compare its accuracy with the commonly-used whole-brain image-based nonlinear registration based on FSL ([Andersson et al., 2010](#)) (we refer to this method as WBR hereafter). We randomly generated 35 subject pairs (with no duplicates) from dataset 2 (see section [Dataset 2 - normal pediatric subjects](#)), with the first subject in the pair being the *fixed* subject and the second subject in the pair being the *moving* subject. For each subject we examined an ensemble

<sup>2</sup> We denote the origin of fiber  $i$ ,  $[x_i, y_i, z_i]$  of  $\{f_i\}$ , as  $O_i$ . We denote the termination coordinate of fiber  $i$ ,  $[x_i, y_i, z_i]$  of  $\{f_i\}$ , as  $T_i$ . A fiber is flipped if  $\|O_1 - O_2\| > \|O_1 - T_1\|$ .

<sup>3</sup> Since the Centerlines of the *moving* and *fixed* bundles have the same number of nodes,  $L$ , we are looking for the optimal rotation matrix ( $R$ ) and translation vector ( $T$ ) between two sets of corresponding 3D points. To do this, we first calculate the centroids,  $C_M$  and  $C_F$ , for the moving and fixed Centerlines, respectively. We then use Singular Value Decomposition of the covariance matrix of the two centered Centerlines to find the rotation matrix,  $R$ , as follows:  $H = \sum_{i=1}^L (Centerline_M^i - C_M)(Centerline_F^i - C_F)^T$ ;  $[U, S, V] = SVD(H)$ . The rotation matrix is then simply  $R = VU^T$ . The translation is  $T = -R \times C_M + C_F$ .

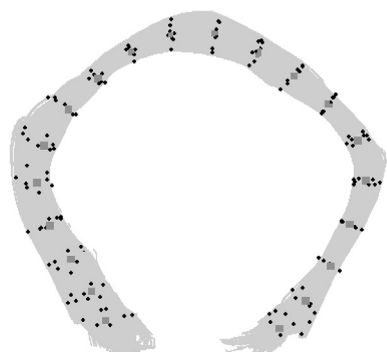


**Fig. 3. Seed Points used in two-step registration.** Example of control points used for the two-step registration on callosum forceps major fiber bundle. Control points for the initial coarse registration along the fibers length step are in gray (diamond shaped), control points used for the fine-registration step are in black (dot shaped).

of eight white matter fiber bundles that were identified using AFQ (see section [White matter fiber bundle identification](#) for details), namely callosum forceps major and minor, left and right corticospinal tracts, left and right inferior fronto-occipital fasciculi and left and right inferior longitudinal fasciculi. The goal of this experiment was to measure the normalized overlap between the registered fiber bundles (IoU, similarly to 23), and to compare it between the two methods. For WBR, we aligned the whole-brain FA maps of the moving subject to the fixed subject in each subject-pair using FMRIB Non-linear Image Registration Tool (FNIRT) (Andersson et al., 2010). First, FMRIB Linear Image Registration Tool 31,32 was used to compute the initial affine transformation of the two FA maps, which was then fed to FNIRT to compute the nonlinear transformation. The resulting nonlinear transformation was applied to the individual fiber bundles of the moving subject using *applywarp* (part of FMRIB Software Library) to obtain the *moved* fiber bundles. The specific parameters used for WBR can be found in [Supplementary Material section Parameters used for WBR](#). For MBR, we directly registered the fiber bundles of the moving subject to the homologous fiber bundles of the fixed subject. The results of this analysis are shown in section [Comparison with nonlinear whole-brain registration \(WBR\)](#).

#### Shape deformation estimation

The registration process moves all the points on the moving bundle such that the bundle is aligned with the reference bundle. This process does not change the number or the order of nodes on the fibers. Thus, the total deformation-per-node can be calculated by simply taking the L2 norm of the euclidean distance between the location of the node pre- and post-registration. In the developmental dataset, the growth along the fibers length is the major contributor to the total deformation, with the radial growth contributing a smaller component. It is also possible to calculate the deformation components in different orientations from the data. However, in this work we focus on the total absolute deformation, regardless of direction.

#### Data for experiments

We demonstrate the methods above on two very different dMRI datasets: (1) we show how a geometric model is created for left thalamic radiation fiber bundle of six adult normal subjects, and how this allows fine-scale correspondence mapping on these bundles (see section [Dataset 1 - normal adult subjects](#) for imaging and data acquisition and pre-processing details); (2) we demonstrate the full pipeline starting from the creation of the geometric model and through estimating shape changes on an ensemble of WM fiber bundles: the occipital and frontal radiation of the corpus callosum - the forceps major (C\_FMajor) and

forceps minor (C\_FMinor) respectively, the inferior fronto-occipital fasciculus (IFOF) and the corticospinal tract (CST) - on a cohort of 38 normal pediatric subjects. The first dataset was acquired for research purposes and is thus of high quality and resolution. This small dataset is used primarily to demonstrate the model. The second dataset was initially acquired for clinical purposes to rule out presence of pathological conditions, and is thus of less good quality. Nevertheless, our methods are applicable and work well on both types of data. For the second dataset, we also show how the shape of white matter fiber bundles changes among subjects of different age and suggest an approximated model for shape change of the analyzed bundles during normal development.

#### Dataset 1 - normal adult subjects

Magnetic resonance imaging diffusion weighted data of six healthy male adults (age 37–39) were acquired at Stanford's Center for Cognitive and Neurobiological Imaging using a 3-T General Electric Discovery 750 MRI equipped with a 32-channel head coil (Nova Medical). Data collection procedures were approved by the Stanford University Institutional Review Board. Written consent was collected from each participant. DWI images were measured at  $1.5 \text{ mm}^3$  uniform spatial resolution with 96 different diffusion directions with  $b$  value of  $2000 \text{ s/mm}^2$  ( $TE = 96.8 \text{ ms}$ ). The images were corrected for spatial distortions due to  $B_0$  field inhomogeneity and motion corrected. Fiber tracking was performed using MRtrix by Tournier et al. (2012).

#### Dataset 2 - normal pediatric subjects

##### Subjects

The subjects chosen for this study were collected from a clinical database of normally developing children with age ranging from 11 days to 8 years. All scans were obtained in the course of normal clinical care based on concerns of the treating physicians and retrospectively reviewed after approval by the Stanford University institutional review board (protocol 28674). Scans were read as normal by the attending pediatric neuroradiologist. Examples of reasons MRI scans were obtained in the normal cohort included: Family history of aneurysm or vascular malformations, sinus disease, peri-orbital dermoid, facial hemangioma, ear infection, and benign strabismus without orbital or intracranial abnormality. The charts of all patients with normal MRIs were interrogated to confirm the absence of any disease states. The total number of subjects was 38, with 21 females and 17 males. The age and gender distributions can be seen in [Fig. 4](#).

##### MRI image acquisition and pre-processing

As part of their clinical evaluation, children were scanned at the Lucile Packard Childrens Hospital at Stanford. Children younger than 3 months of age were scanned using a swaddle-and-feed method; children older than 3 months of age were sedated under general anesthesia; and sedation for children aged 6–8 years was based on individual maturity level and ability to tolerate the MRI exam. High resolution T1-weighted (3D SPGR;  $TR = 7.75 \text{ ms}$ ;  $TE = 3.47 \text{ ms}$ ;  $1 \text{ mm}$  isotropic voxels; orientation = axial) and diffusion-weighted images were obtained at 3T (GE MR750 Discovery; GE Healthcare, Waukesha, WI, USA) using an 8-channel head coil.

Diffusion data were acquired with a twice-refocused GRAPPA DT-EPI sequence ( $TR = 4\text{--}6 \text{ s}$  depending on slice coverage, acquisition matrix =  $128 \times 128$ , acceleration factor = 3, NEX = 3, slice thickness =  $3 \text{ mm}$ , gap =  $0 \text{ mm}$ , FOV =  $20 \text{ cm}$ ) using a  $b$ -value of  $1000 \text{ s/mm}^2$  sampling along 25 isotropically distributed diffusion directions. Five T2-weighted ( $b = 0$ ) images were interspersed throughout the acquisition. To reconstruct the data, we used an automated tailored reconstruction software that selected the best GRAPPA and ghost

calibration weights; performed 3D rigid-body realignment with importance weighting; and employed phase correction and complex averaging to lower Rician noise and to reduce phase artifacts (see [Holdsworth et al., 2012](#) for details). In addition to the 3D realignment procedure, we quantified the degree of translational head motion in each scan by assessing the magnitude (in voxels) of motion correction required for each volume along the x-y-z plane. We chose to remove volumes if translational movement exceeded 2 voxels in any direction. No scan was determined to be unusable due to excessive motion as more than 30% of the total number of volumes were maintained in all children. Using a rigid body transformation, diffusion images were registered via the b0 image to the T1-weighted image that had been manually aligned to a canonical AC-PC orientation. For each voxel, a tensor model was fitted using a standard least-square algorithm. Images depicting fractional anisotropy, mean diffusivity, radial diffusivity and axial diffusivity were generated based on the eigenvalue decomposition of the diffusion tensor [Pierpaoli and Basser, 1996](#). Pre-processing was implemented in MATLAB (MathWorks, Natwick, MI) and the analysis tools are publicly available as part of the Vistasoft git repository, [VistaLab, 2012](#).

#### White matter fiber bundle identification

Automated Fiber Quantification, [Yeatman et al., 2012](#), was used to track and segment cerebral white matter pathways in each subjects native space. In brief, AFQ consists of three main processing steps: i) whole-brain tractography, ii) automatic pathway segmentation, iii) automatic pathway refinement and cleaning. First, a deterministic streamlines tracking algorithm [Mori et al., 1999](#), was used to estimate a whole-brain connectome of fiber bundles. To balance the inclusion of less mature WM regions in very young infants while minimizing the inclusion of GM and partial volume effects, the default tracking parameters were adjusted based on FA values utilized in previous dMRI studies of neonates [Rose et al., 2014](#), [de Brune et al., 2011](#): The tracking algorithm was seeded with a white matter mask defined as all the voxels with FA value above 0.15. Tracking proceeded in all directions and stopped when FA dropped below 0.10 or when the angle between the last path segment and next step direction was greater than 30. Secondly, bundle segmentation was performed using a multiple waypoint ROI procedure in which each fiber from the whole-brain connectome was assigned to a specific fiber group if it passed through two ROIs that defined the trajectory of the fiber group, see [Wakana et al., 2007](#). Because ROIs were defined on a template in MNI space, non-linear transformation, see [Friston and Ashburner, 2004](#), was applied to register these ROIs into each individuals native space.

We defined the central portion of the fiber bundle by clipping each streamline to the portion that spans between the two waypoint ROIs and resampling each fiber bundle to 30 equidistant nodes (see [Fig. 5](#) for example). The final cleaning of the bundle was done by computing the robust mean (3-dimensional Gaussian covariance of the sample points) and removing fibers that were either more than 4 standard deviations above the mean fiber length or that were located more 5 standard deviations away from the core of the fiber bundle. For each child, fiber renderings for the forceps major (C\_FMajor), forceps minor (C\_FMinor), corticospinal tract (CST), inferior fronto-occipital fasciculus (IFOF) and inferior longitudinal fasciculus (ILF) were visually inspected to ensure that each bundle conformed to anatomical norms prior to any statistical/shape analyses.

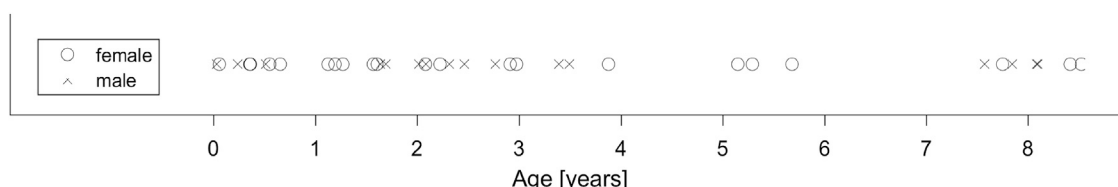


Fig. 4. Age and gender distribution of Dataset 2. Dataset 2 consisted of 38 clinically normal children, with 21 females and 17 males, of age 11 days old through 8.5 years old.

## Experiments and results

We first validate the proposed novel methods by comparing the results of our registration to nonlinear whole-brain image-based registration based on FA (in section [Comparison with nonlinear whole-brain registration \(WBR\)](#)). We then demonstrate the different parts of our framework on the two datasets we elaborated on in section [Data for experiments](#) (sections [Geometric Model](#), [Parcellation](#), [Registration](#), [Deformation mapping](#)). Finally, we present a possible application for estimating the shape change of white matter bundles across different ages (section [Shape deformation model for fiber bundles](#)) (see [Fig. 12](#)).

### Comparison with nonlinear whole-brain registration (WBR)

In this experiment we quantitatively assessed the accuracy of our novel fiber bundle model-based registration (MBR) and compared it with the commonly-used whole-brain image-based nonlinear registration based on FSL ([Andersson et al., 2010](#)) (WBR). [Fig. 6](#) shows the overlap between the *moved* bundle and the *fixed* bundle, as quantified by the IoU index, for each method. Visual inspection of both subplots indicates that our MBR method produces a higher overlap than WBR on all fiber bundles considered in this analysis, except for the callosum forceps minor. T-tests confirmed that our overlap values were significantly higher than those of WBR for all bundles except for FMinor (corrected for multiple comparison, see [supplementary table 1](#)).

### Geometric model

[Fig. 7](#) shows an example of the left inferior fronto-occipital fasciculus of three different subjects, each with its Seed Points. Corresponding Seed Points are plotted with the same color. Visual inspection of the figure allows to qualitatively validate that despite the obvious shape differences between the fiber bundles, both in scale and finer shape details, Seed Points of the same color are located in roughly the same relative location on the bundles, rendering the correspondence mapping correct. The specific values for the four parameters of the geometric model that were used for all experiments in this paper are outlined in section [Geometric model of a fiber bundle](#).

### Parcellation

[Fig. 8](#) shows an example of a bundle parcellation on the left thalamic radiation fiber bundle of three normal adult subjects from dataset 1. Corresponding regions are plotted in the same color across subjects. For ease of visual inspection, we zoom-in to the central portion of the bundle. Even though the shape of the bundles differs from subject to subject, the correspondence is highly reliable in the majority of the bundle. In the regions of the endpoints, due to their irregular nature, there are some inconsistencies. However, it has become standard practice in white matter variability analysis to use only the central portion of the bundles (see e. g. [Yeatman et al., 2012](#)) since the diffusion signal towards the endpoints (either on the cortex or in subcortical structures) is much less reliable than the diffusion signal in the central portion of the bundle. Some tractography tools enable 'clipping' the extracted fiber bundles to the region between the placed seeds, thus avoiding the endpoints region altogether. We demonstrate the method on clipped fiber bundles from

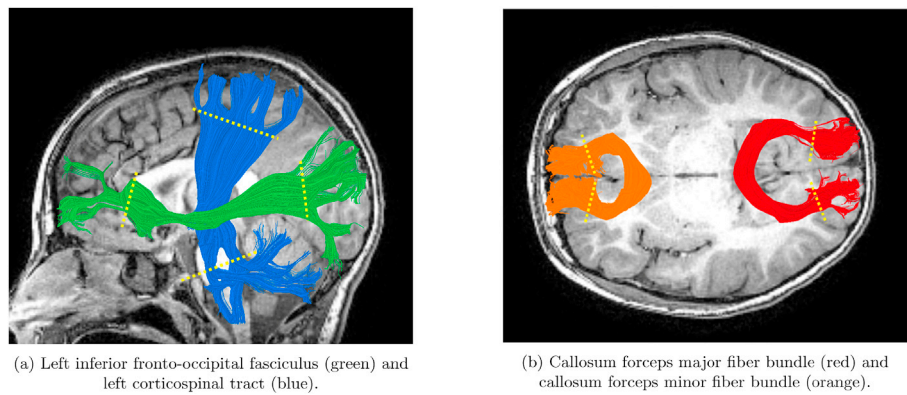


**Fig. 5.** Bundle ROI placement for clipping endpoints on four different bundles. Location of ROIs is indicated by yellow dotted line on each fiber bundle. This procedure was part of the pre-processing prior to the geometry modeling.

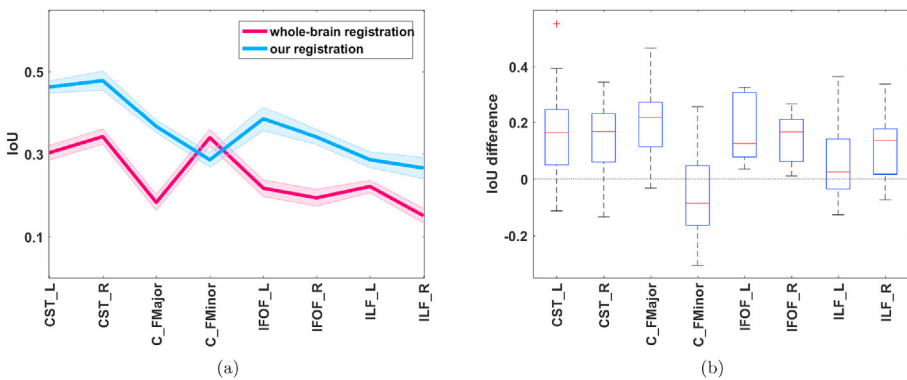


**Fig. 6.** Comparison to FA-based nonlinear Whole-brain based registration. (a) IoU (Intersection over Union) for eight bundles across 35 subject pairs - comparison of WBR and MBR. The plot shows mean values across all 35 pairs are shown in bold lines  $\pm$  one standard error of the mean. (b) Boxplot of the differences in IoU between MBR and WBR. The central mark (red) represents the median, the edges of the box (blue) are the 25th and 75th percentiles, the whiskers extend to the min and max values. Difference values above 0 indicate that MBR performed better.

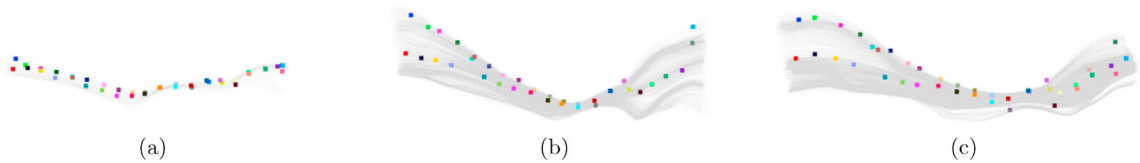


**Fig. 7.** Left inferior fronto-occipital fasciculus of three different subjects with a subset of calculated Seed Points. Seed Points corresponding to the same relative location on the different bundles are plotted using the same color. Visual inspection of the Seed Points proves that the correspondence mapping is correct. (a) 2.8 months old; (b) 2 years old; (c) 7.8 years old.

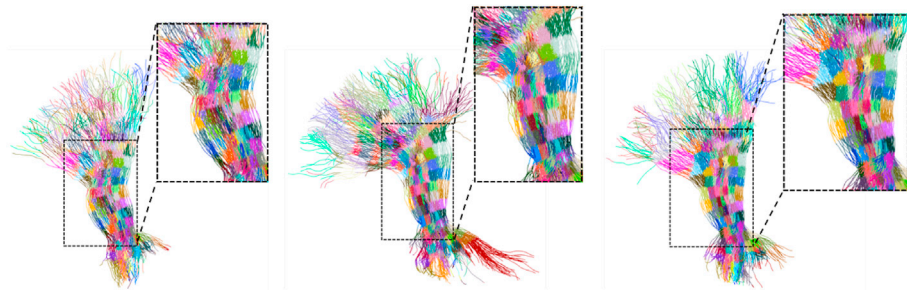


**Fig. 8.** Parcellated Left Thalamic Radiation fiber bundle of three representative subjects from dataset 1. Corresponding regions have the same color across all subjects. In this experiment, no clipping was performed. As a result, it can be seen that while the correspondence mapping at the endpoints has errors, the mapping at the core area of the bundles (shown on the right of each figure) is correct.

dataset 2 below. Fig. 9 shows the resulting parcellation of the left inferior fronto-occipital fasciculus of six different representative subjects from dataset 2. Corresponding ROIs are displayed in the same color. Visual inspection of the images reveals quite satisfactory results - even though

the differences between the shapes are significant, regions at corresponding locations share the same color, meaning that they were mapped correctly.



## Registration

Registration is key tool in medical imaging analysis. It is central to understanding and modeling the shape variability of anatomy structures across subjects. We performed registration between four sets of homologous fiber bundles - callosum forceps major, callosum forceps minor, left IFOF and left corticospinal tract of 38 different subjects. The registration of fiber bundles is evaluated qualitatively by visually inspecting the alignment and quantitatively by comparison to nonlinear whole-brain registration - see section [Comparison with nonlinear whole-brain registration \(WBR\)](#). Fig. 10 shows examples of the registration results we obtain on the callosum forceps major (first row) and left inferior fronto-occipital fasciculus (second row) of an 11 days old infant to a 7.8 years old child. On the left (a) and (d), reference bundles are shown in blue and the "moving" bundle is shown in yellow. The middle figures (b) and (e) show the two bundles after the registration. The right figures (c) and (f) show the "moving" bundle before and after the registration, in purple and yellow colors respectively. As can be seen, after the registration, the "moving" bundle becomes similar in shape and size to the reference bundle.

## Deformation mapping

To better understand how the shape of a fiber bundle changes between subjects of different age, we calculate the total deformation for each node on the fibers. Fig. 11 shows the left IFOF in four different representative subjects from dataset 2, with the nodes of the bundles color-coded according to the magnitude of deformation they undergo during development, with dark red being the highest deformation (about 15 mm) and dark blue being the lowest deformation (0 mm). In this experiment, the left-IFOF of the youngest subject was used as reference and it can be seen that, as expected, the deformation grows with age.

## Shape deformation model for fiber bundles

Regular measurements of head circumference are standard of care for children as abnormalities in head growth can allow for early identification of disease states such as hydrocephalus, [Barbier et al., 2013](#). Normal head growth during early development can be estimated by measuring head circumference and can be approximated for the first several years of life by a logarithmic curve, indicating that the growth is very fast during the first two years of life and gradually slowing until about age 5, when the head size is approximately as in adulthood. It is driven by brain growth which pushes the skull out as the skull fuses. The additional growth is smaller as the skull growth thicker in the following years. Similarly, the same trend can be extracted from our bundle deformation measures. Fig. 12 shows the growth rate (or deformation) as a function of age for four different bundles extracted from the diffusion data of all 38 subjects in dataset 2: callosum forceps major and minor (a) and (b), left corticospinal tract (c) and left inferior fronto-occipital fasciculi (d). As can be seen in the figures, the deformation increases with age. To find whether this increase is best described with a linear or a logarithmic model, we performed 10-fold cross-validation for the deformation data of each bundle. For each bundle, we plot both the best linear and the best

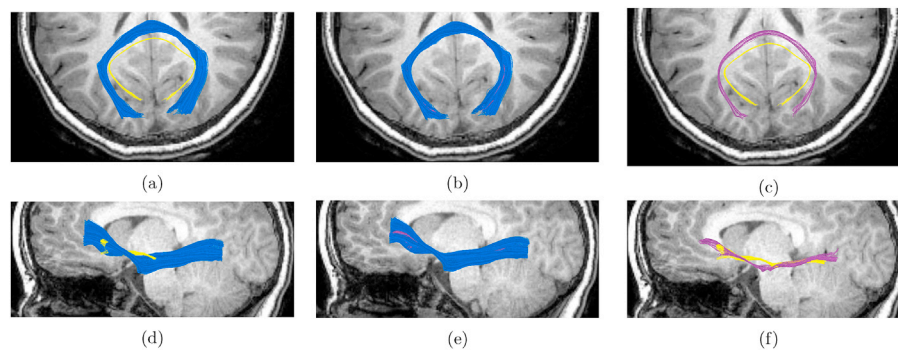
logarithmic model. Logarithmic fitted models are plotted with dashed lines and the linear models are plotted with dotted lines. The equations for the logarithmic and linear models are presented in the caption along with the mean squared error (MSE) for each model. The logarithmic model fits the data better than a linear model for all bundles considered except for the left corticospinal tract, for which the linear model achieves a slightly lower MSE. It is important to note that our pediatric dataset is cross-sectional; therefore, the observed shape deformation cannot solely be associated with age - inter-subject variabilities are also present. Nevertheless, we describe the derivation of the such model primarily to illustrate how our methods can be used to obtain an age-dependent shape deformation model for specific fiber bundles. To generate a model useful for clinical purposes (similarly to the clinically used head circumference measure), a large longitudinal dataset would be required, where several time-points exist per subject. This is further elaborated upon in the discussion section.

## Discussion

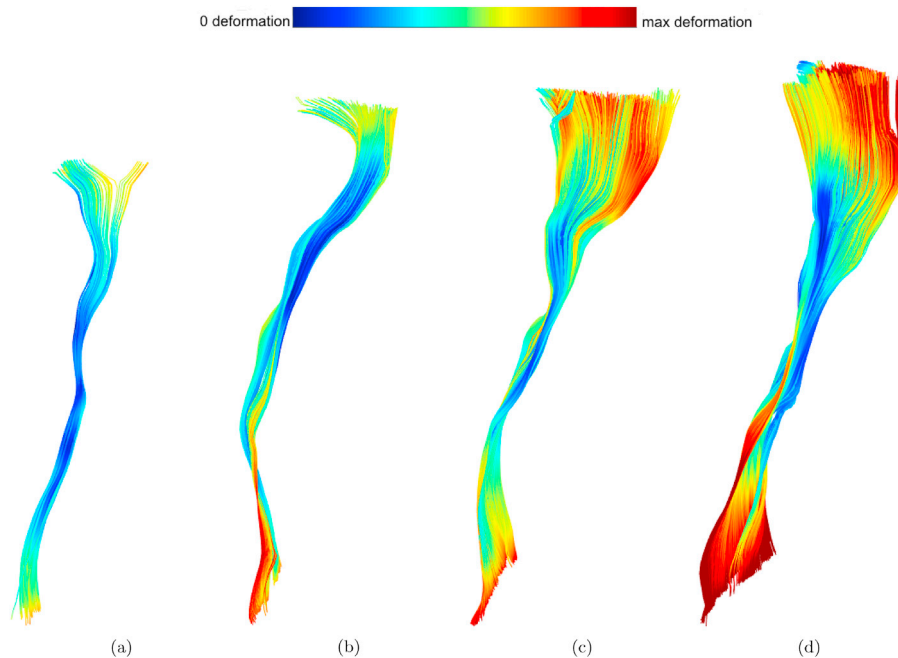
The shape variability of brain structures extracted from T1-weighted data has been studied and modeled extensively. Regional changes in cortical thickness have been linked to a variety of disorders, including schizophrenia, bipolar disorder, depression, Attention Deficit Hyperactivity Disorder (ADHD) and autism spectrum disorders, see e.g. [Rimol et al., 2012](#), [Goldman et al., 2012](#) and [Wang et al., 2016](#). T1 imaging of Alzheimer's patients reveals overall volume loss and shape changes in specific brain structures, such as the hippocampus, amygdala, the ventricles and other regions, see e.g. [Cuingnet et al., 2011](#), [Ferrarini et al., 2006](#), as well as asymmetry in several brain structures, see [Wachinger et al., 2016](#). Shape descriptors of these structures have been used in machine learning algorithms for disease classification, see e.g. [Glozman et al., 2016](#), [Shi et al., 2015](#). The shape variability of the white matter fiber bundles, however, is much less studied. Our work aims to close this gap by providing a set of tools for such analysis. The main goal of this work was to generate a simple and flexible framework for shape analysis of fiber bundles. We demonstrate the utility of such framework by generating an approximation to the normative model of white matter shape change across pediatric subjects. We utilize the 3D shape information of the fiber bundle to create a region-to-region map between fiber bundles of different subjects in a given dataset. The geometric model we propose is flexible and adjustable according to the required analysis - finer or coarser Seed Points placement schemes can be defined. It also has the advantage of a fixed-length representation which makes it suitable for applications of group analysis with deep learning architectures, most of which expect a fixed-size input, as well as more traditional machine learning algorithms. By adjusting only four parameters the user controls the resolution of the model and determines the fineness of the analysis. The methods presented are particularly useful for fiber bundles where the geometry has a major component along the fibers length - e.g. bundles that are relatively long (compared to their cross-sectional 'footprint'). Fiber bundles that have many branches, such as superior longitudinal fasciculus, or bundles that have very short fibers, such as the uncinate fasciculus will not be a suitable candidate for the geometric model we suggest. The geometry of most other major pathways, however, will be



Fig. 9. Parcellated left inferior fronto-occipital fasciculi with clipped endpoints of 6 different subjects from dataset 2. Corresponding regions have the same color across all subjects. Due to the clipping, the endpoints of the fiber bundles are not part of the parcellation scheme, yielding a more accurate correspondence.



**Fig. 10. Registration examples.** Left image in each row shows the moving bundle (in yellow) and the reference bundle (in blue). Middle image in each line shows the two bundles registered. Right image in each line shows the moving bundle before registration (in yellow) and after registration (in purple). Top row shows an example of callosum forceps major fiber bundle registered between a 8.5 year old female and a 4 months old female. Bottom row shows an example of the left inferior fronto-occipital fasciculus (IFOF) registered between an 8.5 year old female and a 21 days old female. In both rows the background is the T1-image of the reference 8.5 year old child, axial plane on the top row and sagittal plane on the bottom row.



**Fig. 11. Shape deformation maps for left inferior fronto-occipital fasciculus color-coded by the amount of deformation in each node.** (a) 21 days old; (b) 2.8 months old; (c) 4.4 months old; (d) 20 months old; (e) 7.8 years old. Blue colors indicate low deformation, red colors indicate high deformation as shown in the colorbar on top. Besides the obvious growth in size, there are also subtle changes in shape that are detected and measured.

well captured with our geometric model. A limitation of our model is that it does not take into considerations 'twisting' of fibers around the central axis, i.e. fiber bundles that have a 'drill-like' structure. Based on what is known about fiber bundle organization in the brain, the occurrence of such structures is not very likely: the seminal paper by Bullmore and Sporns (2012), provides evidence that "many aspects of brain organization can be accounted for by ... minimizing the wiring cost involved in anatomically connecting neurons. ... governed by laws of conservation of time, space and material ...". The brain has limited volume, bound by the skull size. Thus, fiber bundles must travel between brain areas by the optimal path to minimize the volume they occupy. "Swirling" fibers are unlikely, as they would violate this basic principle. Our framework establishes correspondences between regions, enabling accurate localization not only for shape variability analysis, but also for comparison of tissue properties. Many studies have confirmed that tissue properties, such as fractional anisotropy, change along the profile of the fiber bundle. Group analysis of FA changes along bundle profiles were found to be associated with a large number of neurologic conditions including Alzheimer's disease, Parkinson's disease, age related cognitive decline,

Krabbe disease, and delayed neuropsychological effects of treatment of pediatric lymphoid malignancies among others, see Leitner et al., 2015, Feldman et al., 2012a, 2012b, Poretti et al., 2016, Chan et al., 2016, Schuitema et al., 2013 and Teipel et al., 2012. These analyses were enabled by tools such as AFQ by Yeatman et al. (2012), where the authors show how FA profile comparison can be affected by misalignment of the homologous bundles. They propose a simple procedure to roughly align homologous bundles prior to estimation of the FA profile and show that even this rough alignment significantly reduces confounds caused by crossing fibers, and partial voluming with neighboring structures. Our framework allows mapping corresponding regions on fiber bundles in a much finer scale - thus opening the opportunity of performing a more accurate analyses of *localized* tissue properties group comparison and detecting differences that might be easily missed in bundle-averaged or even profile-averaged analysis. We plan to explore this direction in future work. We demonstrated that our methods can be applied to both a high quality research dataset and a clinical dataset, which, by nature of the acquisition protocol, is of lower quality. Our framework extends to a variety of other diffusion models and tractography approaches that

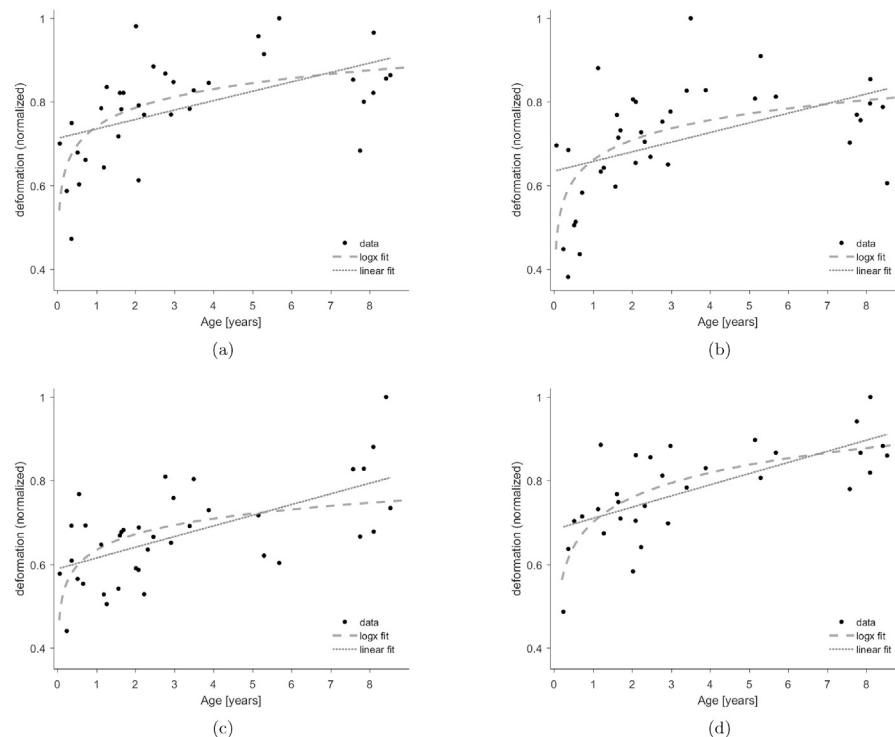


**Fig. 12. Fiber bundle deformation curve data and fitted logarithmic and linear curve for four different pathways.** (a) Callosum forceps major; Logarithmic model:  $y = 0.74 + 0.15 \cdot \log(x)$ . (MSE = 0.008). Linear model:  $y = 0.71 + 0.02 \cdot x$ . (MSE = 0.01). (b) Callosum forceps minor; Logarithmic model:  $y = 0.66 + 0.15 \cdot \log(x)$ . (MSE = 0.011). Linear model:  $y = 0.63 + 0.02 \cdot x$ . (MSE = 0.014). (c) left corticospinal; Logarithmic model:  $y = 0.63 + 0.12 \cdot \log(x)$ . (MSE = 0.008). Linear model:  $y = 0.59 + 0.02 \cdot x$ . (MSE = 0.007). (d) left inferior fronto-occipital; Logarithmic model:  $y = 0.7 + 0.19 \cdot \log(x)$ . (MSE = 0.005). Linear model:  $y = 0.68 + 0.02 \cdot x$ . (MSE = 0.006).

output a similar set of fiber bundles with elongated geometry. We showed that our registration method produces a higher overlap for specific bundles compared to whole-brain FA image-based nonlinear registration. The better registration accuracy of MBR as indicated by higher overlap values is due to the local nature of the applied transformation. As mentioned in sections 2.4 and 2.4.1, in our method the Seed Points on the fiber bundles drive the free-form deformation, which allows a very fine *local* alignment between the fixed and moving bundles. WBR on the other hand creates a deformation field based on voxels intensity values of the 3D volume image - resulting in a less accurate local registration. Our registration and deformation estimation tools create a quantifiable measure for shape difference in the space of fiber bundles. This metric may serve as an additional tool for assessing both individual variability (e.g. in brain lateralization and longitudinal studies) and population variability (e.g. for estimating the normative shape variability per fiber bundle in a cohort of subjects). We have demonstrated in this study how to use our framework to generate an atlas of fiber bundle shape change across different ages for individual white matter pathways. In Singh et al. (2016), the authors show that using a cross-sectional data may estimate a wrong longitudinal effect, since in such dataset, the inter-subject differences are not taken into account. The pediatric dataset we are using is cross-sectional and thus the age-dependent changes we presented need further verification using large-scale longitudinal data. Nevertheless, to the best of our knowledge, this work is the first to suggest a method to derive a model for shape deformation growth for white matter fiber bundles. Applying our analysis to longitudinal data would yield normative growth curves for individual fiber bundles - a measurement may possibly have clinical potential. In future work, we therefore plan to use our framework to assess typical and pathologic development. Further analysis may focus on evaluating recovery following neurosurgical procedures such as tumor extraction or hydrocephalus shunt installation. All the code developed for this work is freely available at <https://github.com/tanyagl/FiberBundleShapeAnalysis>.

## Acknowledgements

TG was supported by Stanford Interdisciplinary Graduate Fellowship; LB was supported by the Stanford Transdisciplinary Initiatives Program, Child Health Research Institute (grant no. 1186741-100-DHDHY); FP was supported by NSF IIS 1636893 and NIH UL1TR001108; DWY was supported by NIH/NINDS R25 Grant, Tashia and John Morgridge Endowed Postdoctoral Fellowship, the Child Health Research Institute and the Stanford NIH-NCATS-CTSA (grant no. UL1 TR001085). KY was supported by the Stanford Transdisciplinary Initiatives Program, Child Health Research Institute. LG was supported by NSF grants IIS-1528025 and DMS-1546206. The authors would like to thank Prof. Brian Wandell and Prof. Heidi Feldman for helpful discussions and suggestions.

## Appendix A. Supplementary data

Supplementary data related to this article can be found at <https://doi.org/10.1016/j.neuroimage.2017.11.052>.

## References

- Agarwal, P., Har-Peled, S., Varadarajan, K., 2005. Geometric approximation via coresets. *Comb. Comput. Geometry* 52.
- Alexander, D., Barker, G., Arridge, S., 2002. Detection and modeling of non-gaussian apparent diffusion coefficient profiles in human brain data. *Magnetic Reson. Med.* 48, 331–340.
- Alexandroni, G., Zimmerman-Moreno, G., Sochen, N., Greenspan, H., 2016. Coresets vs clustering: comparison of methods for redundancy reduction in very large white matter fiber sets. *Med. Imaging 2016. Image Processing*.
- Andersson, J., Jenkinson, M., Smith, S., 2010. Non-linear Registration, Aka Spatial Normalization. *FMRIB Technical Report TR07JA2*.
- Ashburner, J., Friston, K.J., 2000. Voxel-based morphometry: the methods. *NeuroImage* 11 (6), 805–821.
- Barbier, A., Boivin, A., Yoon, W., Vallerand, D., Platt, R., Audibert, F., Barrington, K., Shah, P., Nuyt, A., 2013. New reference curves for head circumference at birth, by gestational age. *Pediatrics* 131.
- Batchelor, P., Calamante, F., Tournier, J., Atkinson, D., Hill, D., Connelly, A., Mar 2006. Quantification of the shape of fiber tracts. *Magnetic Reson. Med.* 55 (4).

- Besl, P., McKay, N., 1992. A method for registration of 3d shapes. *IEEE Trans. Pattern Analysis Mach. Intell.* 14 (2).
- Bullmore, E., Sporns, O., 2012. The economy of brain network organization. *Nat. Rev. Neurosci.* 13 (5).
- Chan, L., Ng, K., Yeoh, C., Rumpel, H., Li, H., Tan, E., 2016. Putaminal diffusivity correlates with disease progression in parkinsons disease: prospective 6-year study. *Medicine* 95 (6).
- Colby, J., Soderberg, L., Lebel, C., Dinov, I., Thompson, P., Sowell, E., 2012. Along-tract statistics allow for enhanced tractography analysis. *NeuroImage* 59.
- Corouge, I., Gouttard, S., Gerig, G., 2004. Towards a shape model of white matter fiber bundles using diffusion tensor mri. In: *Proc. 2004 IEEE International Symposium on Biomedical Imaging: from Nano to Macro*, pp. 1158–1167.
- Cuingnet, R., Gerardin, E., Tessieras, J., Auzias, G., Lehty, S., Habert, M.-O., Chupin, M., Benali, H., Colliot, O., 2011. Automatic classification of patients with alzheimer's disease from structural mri: a comparison of ten methods using the {ADNI} database. *NeuroImage* 56 (2), 766–781. ISSN 1053-8119. Multivariate Decoding and Brain Reading.
- de Brune, F., van Wezel-Meijler, G., Leijser, L., van den Berg-Huysmans, A., van Steenis, A., van Buchem, M., van der Grond, J., 2011. Tractography of developing white matter of the internal capsule and corpus callosum in very preterm infants. *Eur. Radiol.* 21 (3), 538–547.
- Descoteaux, M., Deriche, R., Knosche, T., Anwander, A., 2009. Deterministic and probabilistic tractography based on complex fibre orientation distributions. *IEEE Trans. Med. Imaging* 28, 269–286.
- Durrleman, S., Fillard, P., Pennec, X., Troun, A., Ayache, N., 2011. Registration, atlas estimation and variability analysis of white matter fiber bundles modeled as currents. *NeuroImage* 55 (3), 1073–1090.
- Feldman, H., Lee, E., Loe, L., Yeom, K., Grill-Spector, K., Luna, B., 2012a. White matter microstructure on diffusion tensor imaging is associated with conventional mri findings and cognitive function in adolescents born preterm. *Dev. Med. Child Neurol.* 54 (9), 809–814.
- Feldman, H., Lee, E., Yeatman, J., Yeom, K., 2012b. Language and reading skills in school-aged children and adolescents born preterm are associated with white matter properties on diffusion tensor imaging. *Dev. Med. Child Neurol.* 50 (14), 3348–3362.
- Ferrarini, L., Palm, W., Olofsen, H., van Buchem, M., Reiber, J., Admiraal-Behloul, F., 2006. Shape differences of the brain ventricles in alzheimer's disease. *NeuroImage* 32 (3), 1060–1069.
- Fishbaugh, J., Prastawa, M., Gerig, G., Durrleman, S., 2014. Geodesic regression of image and shape data for improved modeling of 4d trajectories. In: *2014 IEEE 11th International Symposium on Biomedical Imaging (ISBI)*, vol. 55, pp. 385–388.
- Friston, K., Ashburner, J., 2004. Generative and recognition models for neuroanatomy. *NeuroImage* 23 (1), 21–24.
- Garyfallidis, E., Brett, M., Morgado-Correia, M., Williams, G.B., Nimmo-Smith, I., 2012. Quickbundles, a method for tractography simplification. *Front. Neurosci.* 6.
- Garyfallidis, E., Ocegueda, O., Wassermann, D., Descoteaux, M., 2015. Robust and efficient linear registration of white-matter fascicles in the space of streamlines. *NeuroImage* 117, 124–140.
- Glizman, T., Solomon, J., Pestilli, F., Guibas, L., 2016. Shape-attributes of brain structures as biomarkers for alzheimer's disease. *J. Alzheimer's Dis.* 56 (1), 287–295.
- Goldman, A., Pezawas, L., Doz, P., Mattay, V., Fischl, B., Verchinski, B., Chen, Q., Weinberger, D., Meyer-Lindenberg, A., May 2012. Widespread reductions of cortical thickness in schizophrenia and spectrum disorders and evidence of heritability. *Arch. Gen. Psychiatry* 66 (5), 467–477.
- Gori, P., Colliot, O., Marrakchi-Kacem, L., Worbe, Y., De, F., Chavez, M., Poupon, C., Hartmann, A., Ayache, N., Durrleman, S., Dec 2016. Parsimonious approximation of streamline trajectories in white matter fiber bundles. *IEEE Trans. Med. imaging* 35 (12), 2609–2619.
- Groeschel, S., Tournier, J.-D., Northam, G., Baldeweg, T., Wyatt, J., Vollmer, B., Connelly, A., 2014. Identification and interpretation of microstructural abnormalities in motor pathways in adolescents born preterm. *NeuroImage* 87, 209–219.
- Guevara, P., Poupon, C., Riviere, D., Cointepas, Y., Descoteaux, M., Thirion, B., Mangin, J., 2011. Robust clustering of massive tractography datasets. *NeuroImage* 54 (3), 1975–1993.
- Holdsworth, S., Aksoy, M., Newbould, R., Yeom, K., Van, A., Ooi, M., S S, 2012. Diffusion tensor imaging (dti) with retrospective motion correction for large-scale pediatric imaging. *J. Magnetic Reson. Imaging* 36 (4), 961–971.
- Jaccard, P., 1901. Etude comparative de la distribution florale dans une portion des alpes et des jura. *Bull. la Socit Vaudoise Sci. Nat.* 37, 547–579.
- Leitner, Y., Travis, K., Ben-Shachar, M., Yeom, K., Feldman, H., 2015. Tract profiles of the cerebellar white matter pathways in children and adolescents. *Cerebellum* 14 (6), 613–623.
- Mori, S., Crain, B., Chacko, V., van Zijl, P., 1999. Three-dimensional tracking of axonal projections in the brain by magnetic resonance imaging. *Ann. Neurology* 45 (2), 265–269.
- Mori, S., Kageyama, Y., Hou, Z., Aggarwal, M., Patel, J., Brown, T., Miller, M., Wu, D., Troncoso, J., 2017. Elucidation of white matter tracts of the human amygdala by detailed comparison between high-resolution postmortem magnetic resonance imaging and histology. *Front. Neuroanat.* 11.
- O'Donnell, L., Wells, R., Golby, A., Westin, C., 2012. Unbiased groupwise registration of white matter tractography. *Medical image computing and computer-assisted intervention : MICCAI. In: International Conference on Medical Image Computing and Computer-assisted Intervention*.
- Olivetti, E., Sharmin, N., Avesani, P., 2016. Alignment of tractograms as graph matching. *Front. Neurosci.* 10.
- Pierpaoli, C., Basser, P., 1996. Toward a quantitative assessment of diffusion anisotropy. *Magnetic Reson. Med.* 36 (6), 893–906.
- Pierpaoli, C., Barnett, A., Pajevic, S., Chen, R., Penix, L., Virta, A., Basser, P., 2001. Water diffusion changes in wallerian degeneration and their dependence on white matter architecture. *NeuroImage* 13, 1174–1185.
- Poretti, A., Meoded, A., Fatemi, A., 2016. Diffusion tensor imaging: a biomarker of outcome in krabbe's disease. *J. Neurosci. Res.* 94 (11), 1108–1115.
- Rimol, L.M., Nesvåg Jr., R., Årjan Bergmann, D.J.H., Fennema-Notestine, C., Hartman, C.B., Haukvik, U.K., Lange, E., Pung, C.J., Server, A., Melle, I., Andreassen, O.A., Agartz, I., Dale, A.M., March 2012. Cortical volume, surface area, and thickness in schizophrenia and bipolar disorder. *Biol. Psychiatry* 71 (6), 552–560.
- Rose, J., Vassar, R., Cahill-Rowley, K., Guzman, X., Stevenson, D., Barnea-Goraly, N., 2014. Brain microstructural development at near-term age in very-low-birth-weight preterm infants: an atlas-based diffusion imaging study. *NeuroImage* 86, 244–256.
- Schuitema, I., Deprez, S., Hecke, W.V., Daams, M., Uytendaele, A., Sunaert, S., Barkhof, F., van Dulmen-den Broeder, E., van der Pal, E., van den Bos, C., Veerman, A., de Sonneville, L., 2013. Accelerated aging, decreased white matter integrity, and associated neuropsychological dysfunction 25 years after pediatric lymphoid malignancies. *J. Clin. Oncol.* 31 (27).
- Sederberg, J., Thomas, W., Scott, R.P., 1986. Free-form deformation of solid geometric models. *SIGGRAPH Comput. Graph.* 20.
- Shi, J., Stonington, C., Thompson, P., Chen, K., Gutman, B., Reschke, C., Baxter, L., Reiman, E., Caselli, R., Wang, Y., 2015. Studying ventricular abnormalities in mild cognitive impairment with hyperbolic ricci flow and tensor-based morphometry. *NeuroImage* 104 (0), 1–20.
- Silex, V., Davidov, J., Nielsen, J., Fan, Q., Hedden, T., Hollinshead, M., Bustamante, C., Drews, M., Dijk, K.V., Sheridan, M., Buckner, R., Fischl, B., Somerville, L., Yendiki, A., 2017. In: *Registration-free Analysis of Diffusion Mri Tractography Data across Subjects through the Human Lifespan*. ISMRM.
- Singh, N., Hinkle, J., Joshi, S., Fletcher, P.T., March 2016. Hierarchical geodesic models in diffeomorphisms. *Int. J. Comput. Vis.* 117.
- Smith, S., Jenkinson, M., Johansen-Berg, H., Rueckert, D., Nichols, T., Mackay, C., Watkins, K., Ciccarelli, O., Cader, M., Matthews, P., Behrens, T., 2006. Tract-based spatial statistics: voxelwise analysis of multi-subject diffusion data. *NeuroImage* 31 (4), 1487–1505.
- Sotiras, A., Davatzikos, C., Paragios, N., 2013. Deformable medical image registration: a survey. *IEEE Trans. Med. Imaging* 32 (7), 1153–1190.
- Teipel, S., Wegrzyn, M., Meindl, T., Frisoni, G., Bokde, A., Fellgiebel, A., Filippi, M., Hampel, H., Klppel, S., Hauenstein, K., Ewers, M., 2012. Anatomical mri and dti in the diagnosis of alzheimer's disease: a european multicenter study. *J. Alzheimer's Dis.* 31.
- Tournier, D., Calamante, F., Connelly, A., 2012. Mrtrix: diffusion tractography in crossing fiber regions. *Int. J. Imaging Syst. Technol.* 22 (1), 53–66.
- VistaLab, 2012. Mrdiffusion. <http://github.com/vistalab/vistasoft/mrDiffusion>.
- Wachinger, C., Salat, D., Weiner, M., Reuter, M., Oct 2016. Whole-brain analysis reveals increased neuroanatomical asymmetries in dementia for hippocampus and amygdala. *Brain* 139 (12), 32533266. <https://doi.org/10.1093/brain/aww243>.
- Wakana, S., Jiang, H., Nagae-Poetscher, L., van Zijl, P., Mori, S., 2004. Fiber tractbased atlas of human white matter anatomy. *Radiology* 230 (1), 77–87.
- Wakana, S., Caprihan, A., Panzenboeck, M., Fallon, J., Perry, M., Gollub, R., Hua, K., Zhang, J., Jiang, H., Dubey, P., et al., 2007. Reproducibility of quantitative tractography methods applied to cerebral white matter. *NeuroImage* 36 (3), 630–644.
- Wang, T., Wang, K., Qu, H., Zhou, J., Li, Q., Deng, Z., Du, X., Lv, F., Ren, G., Guo, J., Qiu, J., Xie, P., June 2016. Disorganized cortical thickness covariance network in major depressive disorder implicated by aberrant hubs in large-scale networks. *Nat. Sci. Rep.* 6.
- Yeatman, J., Dougherty, R., Myall, N., Wandell, B., Feldman, H., 2012. Tract profiles of white matter properties: automating fiber-tract quantification. *PLoS One* 7 (11).
- Zvita, O., Mayer, A., Shadmi, R., Miron, S., Greenspan, H.K., 2010. Co-registration of white matter tractographies by adaptive-mean-shift and gaussian mixture modeling. In: *IEEE Transactions on Medical Imaging*, vol. 29.